# Modelling and optimisation of single-step laser-based gold nanostructure deposition with tunable optical properties

**Cian Hughes, Ronán McCann, Julen Eguileor, Komal Bagga, Robert Groarke, Fiona Regan, Dermot Brabazon**

## Abstract

As nanotechnology has developed, the creation of nanostructured surfaces has garnered attention for their uses in sensing and catalysis applications. These are however often expensive, time-consuming, and difficult to produce. In contrast, this investigation is focused on the inexpensive, environmentally friendly and fast technique of Confined Atmospheric Pulsed-laser deposition (CAP). The CAP technique has these advantages because it is an atmospheric laser-based direct deposition technique.

Herein, the CAP process is examined in an effort to better understand the process and to begin determining the means to control the properties of the nanostructured surfaces produced by varying the laser fluence and the scan strategy during the ablation. During this investigation, a Nd:YAG laser was applied to deposit gold nanostructures directly onto a polymer substrate. The plasmonic properties and morphologies of the surfaces were examined using UV-Vis spectroscopy and Scanning Electron Microscopy (SEM) respectively. A mathematical model was developed to describe the size and dispersity of the structures deposited and the variation of the position and size of the spectral plasmon peaks in response to the sample processing parameters, with the aim of allowing for a degree of control over these properties and gaining some understanding of the mechanism of this deposition process.

## 1. Introduction

Nanostructured gold surfaces have received much interest from the research community due to their numerous potential applications, in particular as a functional coating for biosensing [1–5], Surface-Enhanced Raman Spectroscopy (SERS) [6,7] and as catalysts [8,9]. Most nanostructures are currently produced by means of chemical based methods in multiple steps [10], or techniques such as Chemical Vapour Deposition (CVD) [11]  or Atomic Layer

30    Deposition (ALD) [12,13]. However, more recently researchers have reported methods for the

31    direct deposition of nanostructures based on the laser ablation of bulk materials [14]. The

32    ablation of these bulk materials results in an ablation plume from which the desired structures

33    condense and are deposited. Common examples of such methods include Pulsed-Laser

34    Deposition (PLD) [15], Laser-Induced Forward Transfer (LIFT) [16] and Laser-Induced

35    Reverse Transfer (LIRT) [17]. These techniques are often (although, less often in the case of

36    LIRT and LIFT) performed in vacuo, to maximise the lifetime of the ablation plume and allow

37    sufficient time for condensation to occur on the deposition substrate [18]. In addition, LIRT

38    and LIFT require the use of expensive and high maintenance femtosecond lasers, increasing

39    the cost of these fabrication methods [17,18]. The laser-assisted fabrication of nanostructured

40    surfaces has also been achieved by the irradiation of thin-films by the process of dewetting

41    [19–21], whereby a thin metal film on a substrate is rapidly melted and then re-solidifies into

42    a nanostructured feature. Dewetting has the advantage of being able to be performed in

43    atmosphere without the need for the use of a femtosecond laser and offers a high degree of

44    morphological control as its mechanism is extremely well understood and is relatively

45    predictable [22] (especially when compared with other methodologies relying on condensation

46    of nanostructures from plasmas). The process of dewetting does, however, somewhat limit the

47    substrates on which the desired nanostructures can be fabricated, requiring the use of substrates

48    with thicknesses on the order of only a few hundred nanometers [19] and high melting points.

49    Often, this substrate is simply Si and $SiO_2$ [19–21] although it is also common to see variants

50    of dewetting that require the use of less cost-efficient materials such as c-plane sapphire [23].

51    Confined Atmospheric PLD (CAP) is a variant of the conventional PLD technique that allows

52    for the deposition of nanostructured metallic thin-films in atmospheric conditions without

53    requiring the use of a femtosecond laser platform [24]. The "confinement" aspect of the CAP

54    method is hypothesised to be its distinguishing feature when compared to conventional PLD.

55    In conventional PLD the quality of a film is generally determined by a Pressure-Distance (PD)

56    scaling law, which states that to obtain a film with given properties $PD^n$ must be a constant

57    (where P is ambient pressure, D is the distance between the target and substrate and n is an

58    exponent determined by experimentation) [25]. This law arises as a result of the fact that

59    increasing plume pressure increases the rate at which particles in that plume dissipate their

60    energy. During PLD high energy particles are necessary for the activation of the substrate

61    surface [25]. Thus if P increases, D must decrease to ensure enough high energy particles reach

62  the substrate. In the case of CAP the atmospheric pressure is much higher than the pressure in

63  standard PLD (which is typically performed at pressures of below 75 mTorr). It follows from

64  this that similar results should be obtainable at atmospheric pressure by greatly reducing the

65  distance. The proposed hypothesis for the mechanism of CAP is that by reducing the distance

66  from several centimetres to only a few microns it comes closer to satisfying this PD scaling

67  law in atmospheric conditions. However, the PD scaling law alone may not entirely be able to

68  account for the deposition observed in the CAP methodology. One possible effect facilitating

69  this process that the PD law alone may not sufficiently capture is the effect of spatial

70  confinement on plasma plumes. The confinement of an ablation plume has been shown to

71  increase its lifetime [26], suggesting that confined plasmas retain their electron temperature for

72  longer. As such, it is possible that this confinement effect helps to ensure that the plume retains

73  enough energy to overcome the activation energy of the deposition substrate, thus facilitating

74  deposition. Should this hypothesised mechanism of CAP as a variant of conventional PLD

75  prove true, it would mean that the morphology of the deposited particles could be strongly

76  influenced by controlling the ambient gas, ambient pressure and target-to-substrate distance

77  [33]. The CAP methodology results in the direct deposition of structures from bulk metal at a

78  rate of 0.3-2.7mm$^2$/s by area (in the parameter range tested during this investigation) and as

79  such is a rapid single step process.

80  Atmospheric PLD (APLD) techniques performed at greater target-substrate distances (and

81  thus, lacking the "confinement" aspect of CAP) have been reported in many applications,

82  generally requiring a significantly longer deposition time to achieve significant depositions

83  [27,28], requiring for example 1800 pulses at 10Hz (i.e. 3 minutes) to deposit a very low density

84  film across a 4mm diameter circular area [27]. Other variants of APLD have been demonstrated

85  avoiding direct deposition from the ejected plume and making use of flowing gases or flowing

86  plasmas to give greater uniformity of particle size and spacing than standard APLD [23]. While

87  this technique compensates for the primary drawback of the atmospheric techniques relative to

88  standard PLD, it does not address the slow deposition rate inherent to most PLD variants that

89  makes them difficult to scale into a process applicable to mass production of nanostructured

90  surfaces. As a result of the relative simplicity and speed of CAP, it is expected that with further

91  study and optimisation this technique has the potential to be a readily-scalable deposition

92  method that does not require an expensive industrial vacuum setup and can be performed with

93  readily available industrial laser platforms.

94  To that end, this study utilises a more consistently reproducible version of the CAP

95  methodology than previously described [24] in a study to determine how various deposition

96  parameters influence the optical and morphological properties of the resulting film. The

97  deposition parameters that were examined were selected based on the criteria that they are

98  factors that can be controlled by a laser-galvanometer processing system thus enabling the

99  derivation of a mathematical process model more relevant to large-scale production process

100 control. These parameters were the fluence of the incident laser beam, the speed of the beam

101 spot raster scan and the spacing between each raster scanned line of the laser spot path . The

102 fluence parameter was chosen because this parameter would be expected to have a significant

103 effect on both the energy of the particles in the ejected plasma plume [26] and the amount of

104 material ablated [15,28]. The scan speed and scan spacing parameters were selected because

105 they determine the amount of spot overlap for successive laser pulses and adjacent scan lines

106 respectively, and as a result they determine the homogeneity of the energy received across the

107 entire scan area [28].

108 The study described was performed with the future goal in mind of applying the CAP technique

109 to the fabrication of biosensors. This goal informed the decisions made regarding which aspects

110 of the characterisation data obtained should be examined. Within the UV/Vis spectroscopy data

111 particular attention was given to the examination of the plasmonic features. Tunable plasmonic

112 properties are extremely useful in the optimisation of SERS [2], Surface Plasmon Resonance

113 (SPR) [4] and UV/Vis spectroscopy [3] biosensing platforms. When examining the SEM

114 images of the obtained nanoparticles both the qualitative morphological features of the films

115 and the quantitative size of the particles deposited were assessed as the morphology [29] and

116 surface area [30] are important factors in maximising the sensitivity of many biosensing

117 platforms.

## 2. Materials and Methods

### 2.1 Materials

120 ZeonorFilm ZF14-188 (Zeon Chemical L.P. Japan) Cyclic Olefin Polymer (COP) was used as

121 the substrate due to its flexibility and high transparency in the UV-NIR range. A 10 mm × 10

122 mm x 0.2mm, 99.9% pure gold metal ablation target was prepared from a sputtering target

123 (Agar Scientific, UK). This target piece was then affixed to a stage, fabricated using PlasClear

124 photopolymer resin and a Freeform Pico (Asiga, CA, USA) 3D printer. The depositions were

125    performed using a 1064 nm diode-pumped, solid state neodymium-doped yttrium aluminium

126    garnet (Nd:YAG) laser. This laser was operated in $TEM_{00}$ mode, producing a beam with a

127    Gaussian profile and a spot diameter of 140µm at the focus. This beam was pulsed at a rate of

128    10kHz and with a pulse width of 700ps. The pulsed laser beam was rastered across the target

129    during sample production using a 2D scanning galvanometer (Raylase SS-12, Germany). The

130    position of the target in the beam waist was controlled using an M-404 4PD nano-position stage

131    (PI, Germany). Design of Experiments (DoE) and data analysis was performed with the aid of

132    StatEase Design Expert 7 and Origin Pro 2016 software packages respectively. Parameters to

133    be examined in the DoE were the laser fluence, the laser scan speed and the raster scan spacing.

134    **2.2 Experimental Setup and Method**

135    The deposition of films for this optimisation study was carried out via the CAP technique,

136    utilising the laser and galvanometer to raster scan the 1064 nm laser beam with a 10 kHz pulse

137    repetition frequency across the across the surface of the gold foil target through a COP

138    substrate, see Figure 1.



139
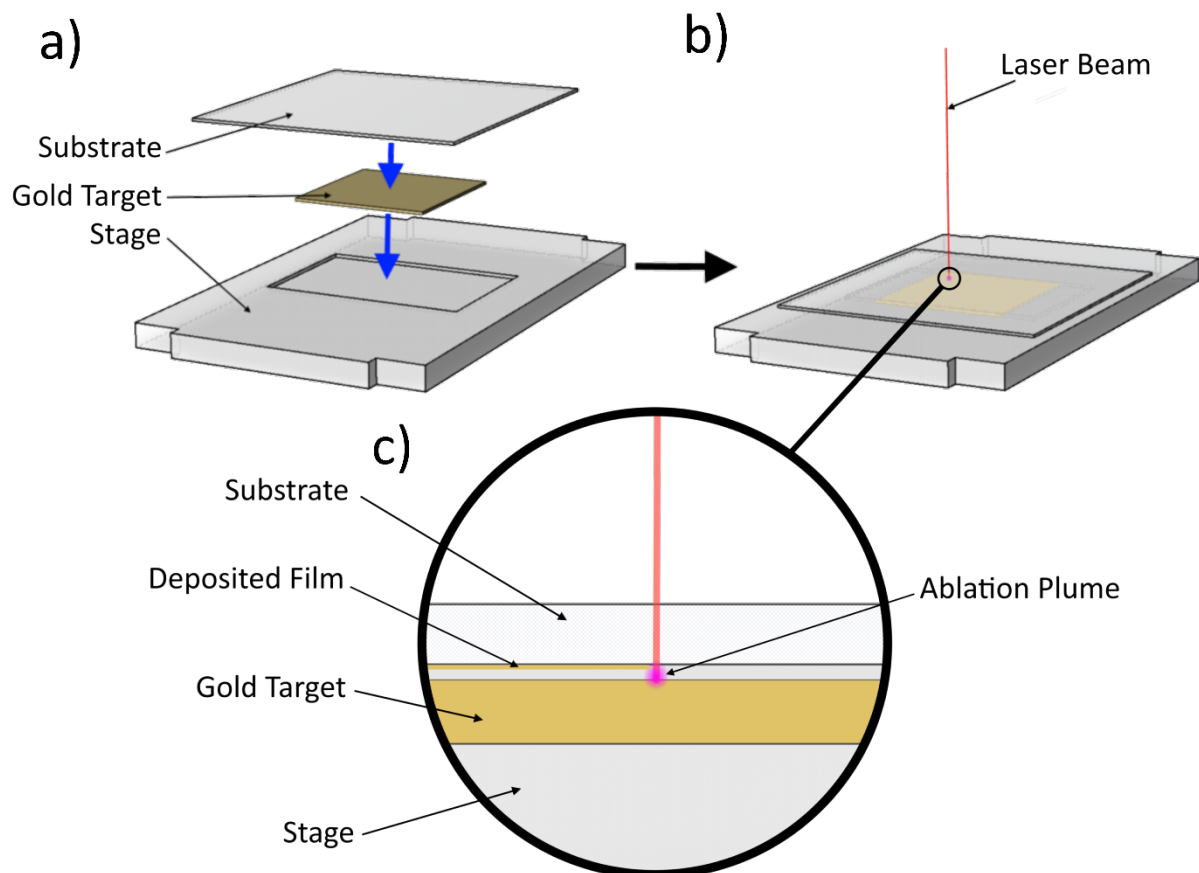
**Fig. 1.** Schematic of a CAP experimental setup representing the deposition of a gold nanostructured film onto a substrate.

The target was adhesively affixed to the stage at a depth 50 μm beneath the substrate. The beam was unidirectionally rastered across the target (travelling unidirectionally for each individual scanline) in a 5 x 5 mm square pattern. Thus, once the raster scan pattern was completed a 5mm x 5mm square area of nanostructured gold thin-film had been deposited. These parameters were selected according to a 2-level and 3 factor factorial DoE; and the resulting sample set was produced in duplicate for variance assessment. Numerous samples were prepared using this method to examine the effects of fluence (from 0.221 $J/cm^2$ to 0.481 $J.cm^2$), scan spacing (that is, the gap between each raster scanned line, varied from 50 μm to 150 μm) and scan speed (from 6 mm/s to 18 mm/s) on the films deposited.

### 2.3 Film Characterisation

The resulting samples were characterised via UV-Vis spectroscopy (Agilent, Cary 50, USA). Samples were carbon coated using a Scancoat Six (Edwards, UK) with carbon evaporation accessory at a pressure of $10^{-4}$ bar for examination via Scanning Electron Microscopy (SEM) using an Evo LS15 (Carl Zeiss AG). Image analysis on the SEM images obtained was carried out using Fiji image analysis software [31]. The resulting data was input into the DoE to develop a mathematical model that would allow for process understanding and control.

### 3. Results and Discussion

The test samples were successfully prepared in atmospheric conditions, at room temperature using only the gold target, 2D motorized stage, COP substrate and 1064nm laser. Such a practical example of this simple, direct methodology working as described suggests that this technique is an environmentally friendly alternative to many existing techniques. In addition, the depositions were performed with ablation times ranging from 9 seconds (scan speed: 18 mm/s, scan spacing: 150 μm) to 83 seconds (scan speed: 6mm/s, scan spacing: 150 μm) for the deposition of the square of 25 $mm^2$ area. The exact deposition parameters and sample numbers used during this investigation are listed in Table 1.

**Table 1.** A list of the deposition parameters for samples with multiple samples produced for each combination of parameters.

| Sample numbers | Fluence (J/cm$^2$) | Scan Speed (mm/s) | Scan Spacing (µm) |
| --- | --- | --- | --- |
| 1, 14 | 0.221 | 6 | 50 |
| 2, 15 | 0.221 | 18 | 50 |
| 3, 16 | 0.481 | 6 | 50 |
| 4, 17 | 0.481 | 18 | 50 |
| 5, 18 | 0.221 | 6 | 150 |
| 6, 19 | 0.221 | 18 | 150 |
| 7, 20 | 0.481 | 6 | 150 |
| 8, 21 | 0.481 | 18 | 150 |
| 9, 10, 11, 12, 13, 22, 23, 24, 25, 26 | 0.351 | 12 | 100 |

The samples resulting from these depositions appeared as squares on the COP substrate, ranging in colour from red to brown. The deposited films appeared matte when in a face-up orientation, and appeared shiny when viewed from the opposite side. When examined closely it seems apparent that the metal-polymer interface is smooth and reflective, leading to this observed difference in appearance. The resulting characterisation data was then analysed to find any statistically significant relationships between the process parameters and the properties of the films produced.

**3.1 Film Morphology**

SEM analysis showed the formation of nanostructures for all parameters tested. These structures shared a similar morphology, being comprised of smaller, fused or aggregated nanoparticles. Upon further examination, a degree of variation was noted in the size of these structures and the homogeneity of their deposition at differing ablation parameters (Figure 2).
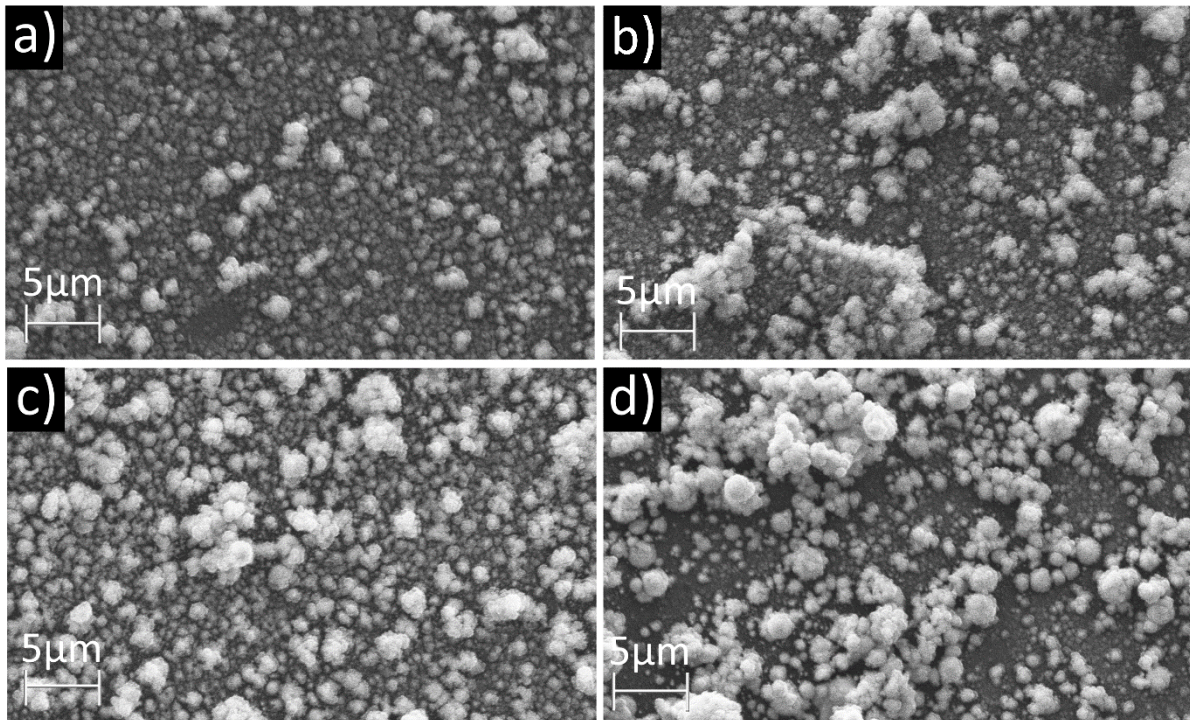
**Fig. 2.** SEM images of samples a) 18 (6 mm/s, 0.221 J/cm$^2$, 150 μm), b) 11 (12 mm/s, 0.351 J/cm$^2$, 100 μm), c) 20 (12 mm/s, 0.481 J/cm$^2$, 150 μm) and d) 4 (18 mm/s, 0.481 J/cm$^2$, 50 μm) at 8380× magnification.

While similar structures to those shown in Figure 2 were present in every sample, the specific images shown were chosen because they exhibit some of the clearest examples of the structures discussed herein. Figure 2a is an example of a more homogenous film obtained at lowest fluence, lowest scan speed and highest scan spacing (6 mm/s, 0.221 J/cm$^2$, 150 μm), clearly showing less large-scale aggregation and fewer large spheroidal structures than other films presented. In contrast, Figures 2b and 2c show less homogenous films, with 2b showing evidence of large aggregated structures forming and 2c showing even more aggregate formation than 2b. Figure 2d shows an example of a film comprised of a mix of nanoparticles, micro-scale nanoparticle aggregates and larger spheroidal microparticles. It is hypothesised that the larger spheroidal microparticle structures observed in Figure 2d may be the result of the laser melting and sintering of deposited micro-scale nanoparticle aggregates into the spheroidally lobed structures present [32]. The aggregated structures apparent with a broccoli-like appearance would suggest that the deposited film has a high ratio of surface area to volume, a property that is extremely desirable for their proposed application in biosensors [33].

200    All parameter sets within the window tested resulted in a densely packed nanostructured film.

201    As mentioned previously some parameters (e.g. sample 18, Figure 2a) resulted in relatively

202    uniform films while other parameters (e.g. sample 4, Figure 2d) resulted in aggregated clusters

203    of varying size.

204    Following this, the SEM images obtained were analysed by manual particle sizing. During

205    particle sizing fifty particles from each sample were chosen using a script that randomly placed

206    points on the image. The particles marked by these points were then sized by manual ellipse

207    fitting to obtain a major axis, minor axis, area and eccentricity measurement for each. Average

208    responses were calculated for each sample based on the fifty random particles measured in their

209    respective SEM images (Table 2). Standard deviations are also presented as a measure of the

210    dispersity of the particles produced.

211

212    **Table 2.** Particle size analysis results (with standard deviation indicated, n=50).

| Sample | Avg Minor Axis (nm) | Avg Major Axis (nm) | Avg Area ($nm^2$) | Avg Eccentricity |
|---|---|---|---|---|
| 1 | $220 \pm 60$ | $280 \pm 80$ | $206700 \pm 114200$ | $0.51 \pm 0.24$ |
| 2 | $150 \pm 40$ | $180 \pm 50$ | $87600 \pm 49300$ | $0.46 \pm 0.27$ |
| 3 | $200 \pm 50$ | $240 \pm 60$ | $162700 \pm 86400$ | $0.36 \pm 0.29$ |
| 4 | $230 \pm 60$ | $280 \pm 70$ | $217600 \pm 109500$ | $0.44 \pm 0.26$ |
| 5 | $220 \pm 50$ | $260 \pm 70$ | $188400 \pm 99400$ | $0.45 \pm 0.25$ |
| 6 | $210 \pm 50$ | $260 \pm 60$ | $178900 \pm 88100$ | $0.48 \pm 0.25$ |
| 7 | $190 \pm 50$ | $210 \pm 60$ | $134300 \pm 77800$ | $0.31 \pm 0.28$ |
| 8 | $240 \pm 90$ | $270 \pm 100$ | $223400 \pm 210200$ | $0.35 \pm 0.28$ |
| 9 | $270 \pm 90$ | $320 \pm 110$ | $300800 \pm 205300$ | $0.52 \pm 0.20$ |
| 10 | $270 \pm 80$ | $290 \pm 90$ | $243300 \pm 143100$ | $0.40 \pm 0.30$ |
| 11 | $330 \pm 130$ | $390 \pm 150$ | $458500 \pm 430000$ | $0.50 \pm 0.23$ |
| 12 | $250 \pm 80$ | $290 \pm 80$ | $244400 \pm 135800$ | $0.40 \pm 0.29$ |
| 13 | $230 \pm 70$ | $270 \pm 80$ | $212700 \pm 126100$ | $0.40 \pm 0.29$ |
| 14 | $280 \pm 110$ | $310 \pm 130$ | $314300 \pm 251500$ | $0.36 \pm 0.28$ |
| 15 | $280 \pm 90$ | $320 \pm 100$ | $303500 \pm 185700$ | $0.37 \pm 0.27$ |
| 16 | $260 \pm 100$ | $300 \pm 120$ | $275400 \pm 241700$ | $0.44 \pm 0.26$ |
| 17 | $240 \pm 110$ | $280 \pm 120$ | $250000 \pm 248800$ | $0.46 \pm 0.25$ |
| 18 | $210 \pm 60$ | $250 \pm 70$ | $179000 \pm 104200$ | $0.42 \pm 0.29$ |
| 19 | $180 \pm 50$ | $210 \pm 60$ | $128800 \pm 71500$ | $0.44 \pm 0.27$ |
| 20 | $200 \pm 40$ | $240 \pm 50$ | $157400 \pm 61200$ | $0.41 \pm 0.28$ |

| | | | |
|---|---|---|---|
| 21 | 230 ± 80 | 270 ± 90 | 214200 ± 141200 | 0.44 ± 0.27 |
| 22 | 200 ± 50 | 240 ± 50 | 154800 ± 67600 | 0.41 ± 0.28 |
| 23 | 320 ± 90 | 380 ± 100 | 398000 ± 231100 | 0.49 ± 0.19 |
| 24 | 230 ± 60 | 260 ± 60 | 196900 ± 103800 | 0.37 ± 0.29 |
| 25 | 200 ± 40 | 230 ± 50 | 143600 ± 67600 | 0.41 ± 0.28 |
| 26 | 230 ± 70 | 290 ± 90 | 223100 ± 131800 | 0.51 ± 0.25 |

## 3.2 Optical Properties

The deposited films were also examined using UV-Vis spectroscopy. These spectra were obtained to examine the plasmonic properties of the films and to allow for an examination of the effect of various ablation parameters on those resulting plasmonic properties. Following analysis, the UV-Vis spectra obtained from these samples were then subjected to baseline correction (to remove the broad background peak due to the ablated COP) and peak analysis. This analysis was used to find the local maxima (suggested to be largely indicative of particle size [34]) and the area under the peak (i.e. its intensity, suggested to be indicative of the relative thickness of the film deposited [35]). The spectra obtained showed broad plasmonic peaks in the 530 nm to 580 nm range, with a distinctive shape that tapers off more gradually on the longer wavelength side of the peak than it does on the shorter wavelength side. This skewing is evident in the minima observed for the peaks obtained. The shorter wavelength minima of the peaks (on the left side of the spectrum as graphed) observed were at approximately 450 nm, which is 105 nm from the median of the range in which the maxima were found (555 nm). Meanwhile the longer wavelength minima (on the right side of the spectrum as graphed) were generally close to 800nm, which is 245 nm from the median of the range for the maxima. Figure 3 shows an example of a typical UV-Vis spectrum obtained, as well as baseline corrected peaks for several samples exhibiting the variations observed in peak position and intensity.

**Table 3.** Results of peak analysis performed on the UV-Vis spectrum of each individual sample.

| Sample no. | Plasmonic Peak Wavelength (nm) | Plasmonic Peak Integral | Plasmon Peak Full Width at Half Maximum (nm) |
|---|---|---|---|
| 1 | 561 | 28.1 | 160 |
| 2 | 568 | 26.3 | 151 |

| | | | |
|---|---|---|---|
| 3 | 570 | 47.7 | 146 |
| 4 | 576 | 40.9 | 170 |
| 5 | 551 | 11.1 | 147 |
| 6 | 550 | 12.3 | 138 |
| 7 | 572 | 35.6 | 163 |
| 8 | 574 | 26.1 | 152 |
| 9 | 568 | 21.8 | 161 |
| 10 | 571 | 23.3 | 164 |
| 11 | 568 | 22.3 | 164 |
| 12 | 577 | 49.9 | 225 |
| 13 | 576 | 30.4 | 193 |
| 14 | 562 | 33.1 | 161 |
| 15 | 559 | 15.6 | 151 |
| 16 | 564 | 38.9 | 146 |
| 17 | 579 | 45.1 | 163 |
| 18 | 559 | 18.5 | 154 |
| 19 | 557 | 21.2 | 150 |
| 20 | 578 | 42.7 | 169 |
| 21 | 566 | 34.5 | 134 |
| 22 | 568 | 29.8 | 155 |
| 23 | 568 | 33.5 | 142 |
| 24 | 570 | 32.5 | 151 |
| 25 | 568 | 25.0 | 146 |
| 26 | 572 | 28.8 | 164 |

234
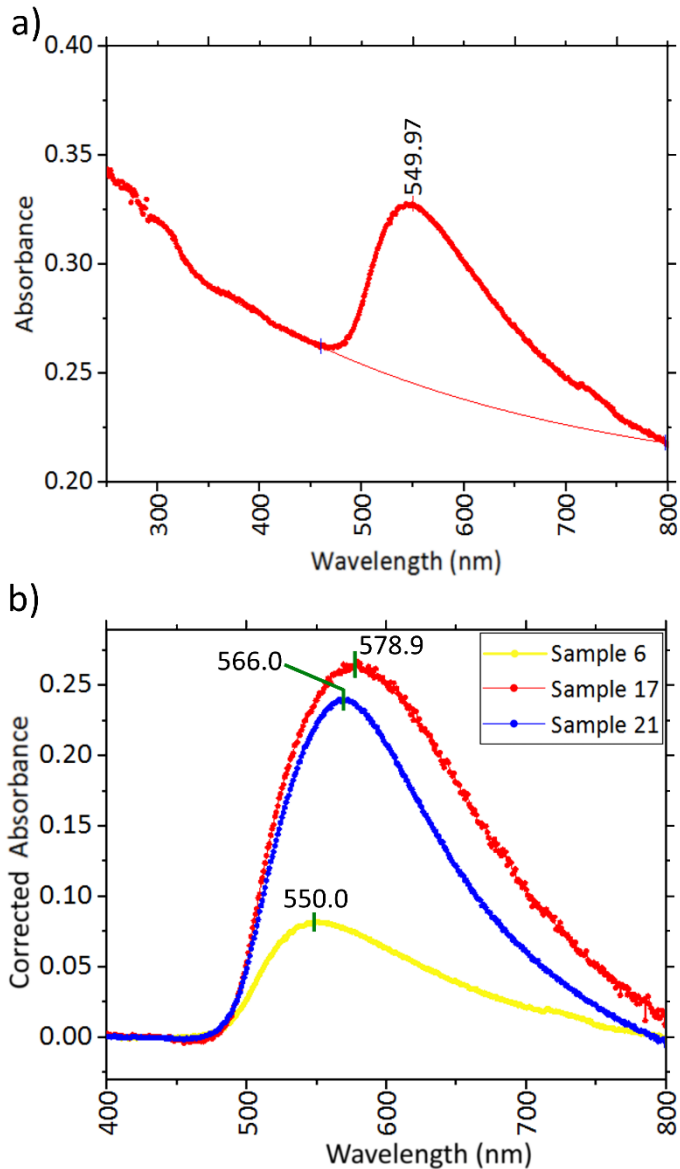
**Fig. 3.** Typical UV-Vis spectra of the samples obtained after CAP deposition of gold nanostructures onto COP showing a) The UV-Vis spectrum of sample 6 showing the corrected baseline and the plasmonic peak at around 550 nm; and b) UV-Vis spectra of samples 6, 17 and 21 exhibiting varying intensities of peaks ranging from 550 nm to 578 nm obtained at different CAP parameters.

The broad background feature in the UV-Vis spectra obtained are likely a result of the effects of the laser on the COP substrate. Based on previous investigations, the effects of a direct incident laser beam focussed on COP at the selected fluences are understood to result in a small degree of polymer oxidation (in the form of carbonylation) and the ablation of channels with a depth of up to approximately 40μm and a width of up to approximately 120μm [36].

246 Additionally, studies involving the deliberate oxidation of various similar COP samples
247 resulted in the formation of carbonyl groups and comparable features in the UV-Vis spectra
248 observed [37]. Based on this it is reasonable to expect that the effects of such a laser on COP
249 placed 50µm above the focal point would be similar and that the resulting oxidation is the
250 source of the broad baseline peak.

**3.3 Signal-to-Noise Ratio Analysis**

252 During analysis, a signal-to-noise (SNR) value was calculated for each experimental output
253 recorded. This SNR value was calculated to determine the contribution of random noise in each
254 output dataset. As such, these SNR values provide a means for assessing how accurately the
255 instruments and methodologies used during characterisation were able to measure the response
256 values. As the data obtained falls within the scope of image processing and analytical chemistry
257 (specifically, spectroscopic analysis) it was decided that the SNRs should be calculated using
258 the formulae considered standard in these fields. In image processing (with the exception of
259 direct electronic signal analysis) SNR is most often calculated using minor variations on the
260 true SNR formula [38,39] (that is the mean signal ($\mu$) over the standard deviation of the dataset
261 ($\sigma$) [40]). The "true SNR" formula is also commonly used in analytical chemistry [40]. As such,
262 it was decided the SNR of the collected data should also be calculated using the true SNR
263 formula. The resulting SNRs were then converted to decibels by the application of a
264 logarithmic operation. As such, all SNR values for each dataset were calculated according to
265 the following formula:

266 $SNR = 10(\log_{10}(\mu/\sigma))$

267 The signal to noise ratio was calculated for each response measured during the course of this
268 study and the results can be seen in Table 4.

269 **Table 4.** The calculated mean signal, standard deviation and signal-to-noise ratio of each
270 response dataset collected.

| | Mean Signal | Standard Deviation | Signal-to-Noise Ratio (dB) |
|---|---|---|---|
| Plasmonic Peak Position (nm) | 567 | 7.8 | 18.6 |

13

| | | | |
|---|---|---|---|
| Plasmonic Peak Integral | 29.8 | 10.4 | 4.6 |
| Plasmonic Peak FWHM (nm) | 159 | 18.1 | 9.4 |
| Average Minor Axis (nm) | 230 | 40 | 7.7 |
| Minor Axis Standard Deviation (nm) | 70 | 20 | 4.5 |
| Average Major Axis (nm) | 270 | 50 | 7.6 |
| Major Axis Standard Deviation (nm) | 80 | 30 | 4.8 |
| Average Area ($nm^2$) | 223000 | 82800 | 4.3 |
| Area Standard Deviation ($nm^2$) | 145500 | 85500 | 2.3 |
| Average Eccentricity | 0.43 | 0.055 | 8.9 |
| Eccentricity Standard Deviation | 0.27 | 0.027 | 10.0 |

271

272 The SNR analysis results show that the plasmonic peak position output gave the strongest
273 response relative to noise suggesting that this value was most accurately quantified by the
274 instruments and characterisation methods used. Conversely, the area standard deviation
275 response gave the lowest response relative to noise.

276 **3.4 Analysis of Variance (ANOVA)**

277 With the aid of Design Expert 7 DOE software, each of the output datasets were examined to
278 derive models relating the processing parameters to the resulting responses. From the responses
279 recorded four statistically significant model equations were derived describing the effects
280 influencing the observed area of the deposited particles (representative of their size), the
281 standard deviation of those area measurements (representative of the particle dispersity), the
282 plasmonic peak position and the plasmonic peak integral. The full results of the ANOVA
283 analyses for these models are shown in Table 5.

284  **Table 5.** The ANOVA ouptuts for each of the models derived. More detailed tables are
285  available in the ESI.

| Response | Degrees of Freedom | Adjusted $R^2$ | Predicted $R^2$ | Adequate Precision | F Value |
|---|---|---|---|---|---|
| Particle Area | 7 | 0.4952 | 0.2850 | 8.682 | 4.50 |
| Area Standard Deviation | 7 | 0.4985 | 0.3312 | 8.021 | 4.55 |
| Plasmonic Peak Position | 5 | 0.5922 | 0.4085 | 9.528 | 8.26 |
| Plasmonic Peak Integral | 2 | 0.5990 | 0.5380 | 12.440 | 19.67 |

286

287  The ANOVA results for each of these derived models found that both size models have an
288  adjusted $R^2$ of approximately 0.5, while each plasmonic peak based model has an adjusted $R^2$
289  of greater than 0.59. All models were found to have an adequate precision of greater than 8,
290  which is well in excess of the desired value of at least 4 for a statistically significant model
291  [41]. The F-value for the model describing the plasmonic peak integral is large (19.67). The F-
292  value of the plasmonic peak position model (8.26) is smaller but still significant. Both particle
293  size related models have an F value of ~4.5, which are also statistically significant values.

294  The ANOVA tables presented provide a great deal of information about the models derived
295  when considered within the context of the SNR values of the outputs examined. The relatively
296  high SNR of the plasmonic peak position data (18.63 dB) suggests that this model is significant.
297  Considering this fact, and that the F-value of the peak position model is lower than would be
298  expected for such a correlated, high SNR and high adequate precision model it seems likely
299  that the inclusion of an independent variable for scan speed in the model is increasing the
300  observed variance. The scan speed was, however, found to have a statistically significant
301  interaction with the scan spacing and due to the hierarchical DoE modelling system used this
302  necessitated the inclusion of the independent scan speed variable. Conversely, the lower but
303  still acceptable SNR for the plasmonic peak integral (4.581) with a higher F-value suggests
304  that the observed variance in the data is primarily a result of noise. Similarly, the SNR values
305  of the area and standard deviation of area models (4.301 and 2.310 respectively) suggest much

306 of the observed variance in these models is due to noise, while the lower F value suggests that
307 these models are the least statistically significant of all the models obtained. The higher levels
308 of noise observed in some datasets could be reduced by further expanding the process space
309 being examined with the inclusion of an increased quantity of repeated sample characterisation
310 data at the tested processing parameters..

311

312 **3.5 Particle Morphology Models**

313 With the aid of ANOVA analysis performed by DoE software, two statistically significant
314 mathematical models were found describing features related to the morphology of the particles
315 deposited (Figure 4). The first relationship found describes an inverse squared relationship
316 between the area of the deposited particles (A) and all processing parameters measured. In this
317 case the area serves as a measurement of the size of the particles, as the area of the particles on
318 an SEM image should be proportional to their size. The derived equation is as follows:

319 $A = (-1.32e^{-4}v - 5.18e^{-3}F - 1.52e^{-5}d + 4.15e^{-4}vF - 1.95e^{-6}vd + 6.04e^{-5}Fd + 5.62e^{-6}vFd + 3.30e^{-3})^{-2}$
320

321 This equation suggests that the strongest contribution to the size of the particles is made by the
322 fluence parameter (F). This model equation also suggests that there are many interactions
323 between the selected processing parameters that also influence the particle size, including a
324 complex 3-way interaction between fluence, scan speed (v) and scan spacing (d), as shown by
325 the presence of the vFd component of the equation.

326 This analysis also yielded an equation describing the influence of the processing parameters on
327 the standard deviations of the areas of the deposited particles ($\sigma_A$). Given that the area of the
328 particles serves as a measurement of their size, the standard deviation of the areas should thus
329 serve as a suitable measurement of the dispersity of the deposited particles (i.e. the
330 homogeneity of the film). As such, an inverse cubed relationship between the processing
331 parameters and the dispersity of the particles was found according to the following equation:

332 $\sigma_A = (-7.23e^{-4}v - 0.044F - 1.15e^{-4}d + 2.39e^{-3}vF + 1.21e^{-5}vd + 5.11e^{-4}Fd - 3.69e^{-5}vFd + 0.029)^{-3}$
333

Similar to the equation describing the area of the particles, this equation suggests that the dispersity is primarily influenced by the fluence of the incident laser and that there are many interactions present.
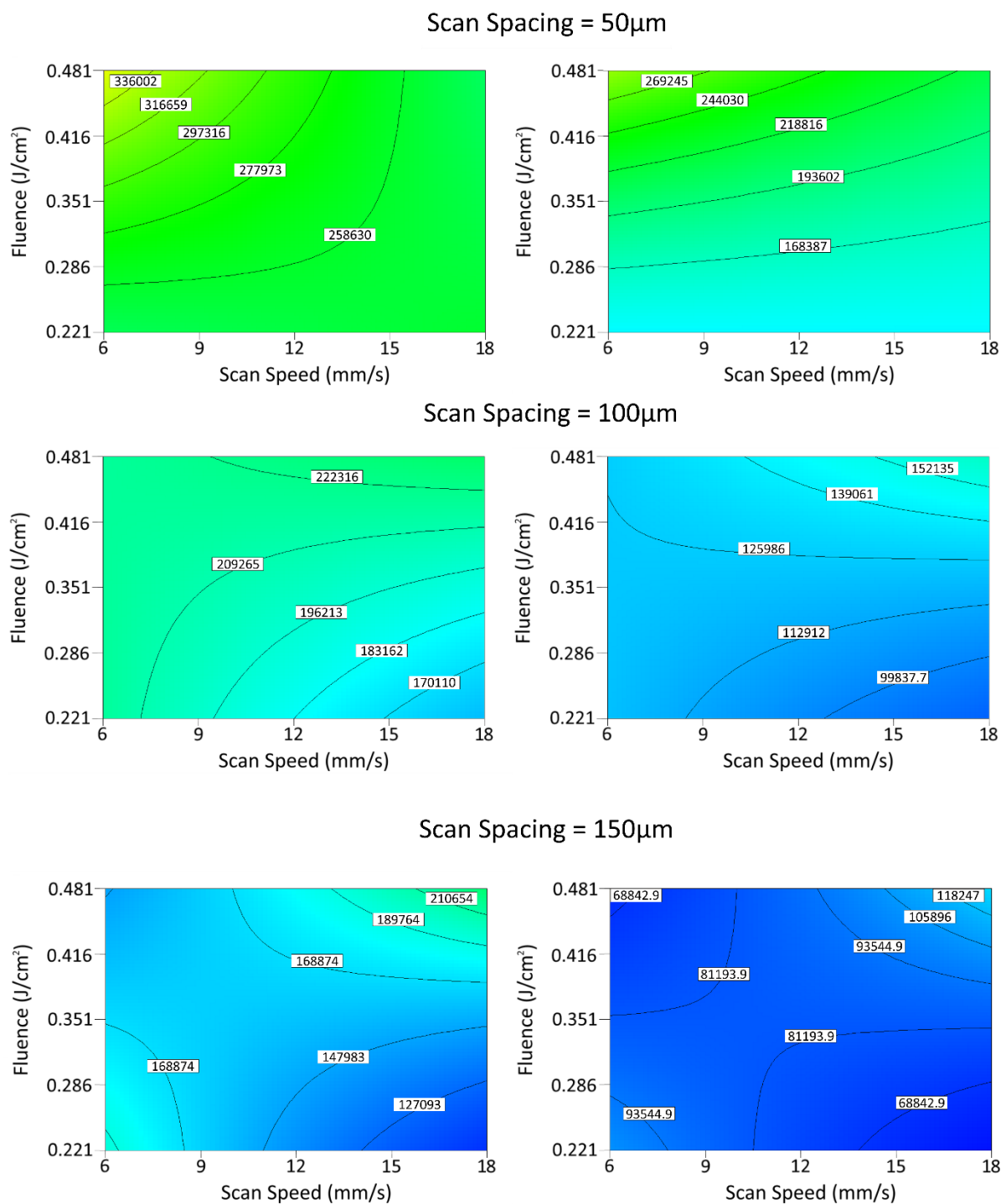


**Fig. 4.** Contour plots of the areas (left) and the standard deviations of areas (right) predicted by the derived models based at various scan spacings (50μm, 100μm and 150μm)

The agreement of this model with the practical results was evaluated with the aid of a normal plot of its residuals and a plot of predicted vs actual values (Figure 5). It can be seen from these graphs that deviations from the model are approximately normal and there are no significant outliers in either dataset.
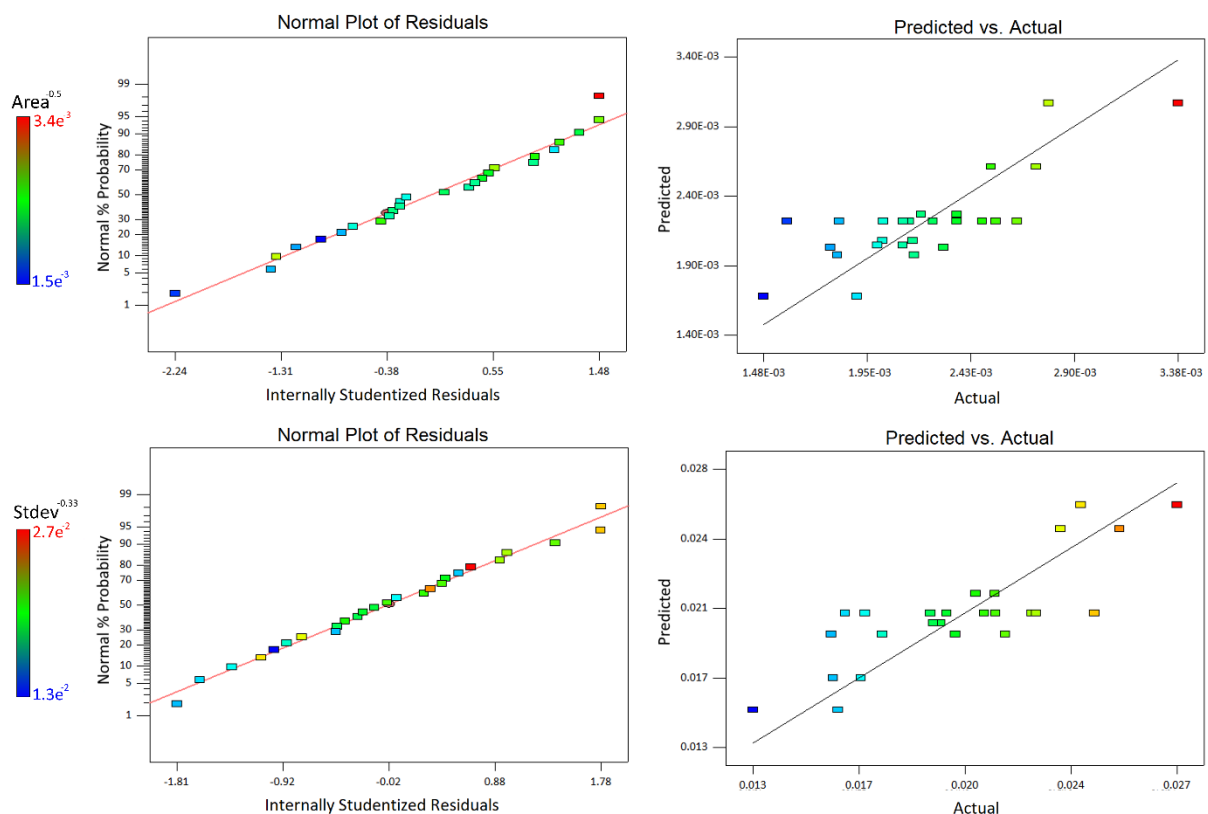


**Fig. 5.** The normal plot of residuals and predicted vs actual plot for the size model derived (top) and the dispersity model derived (bottom).

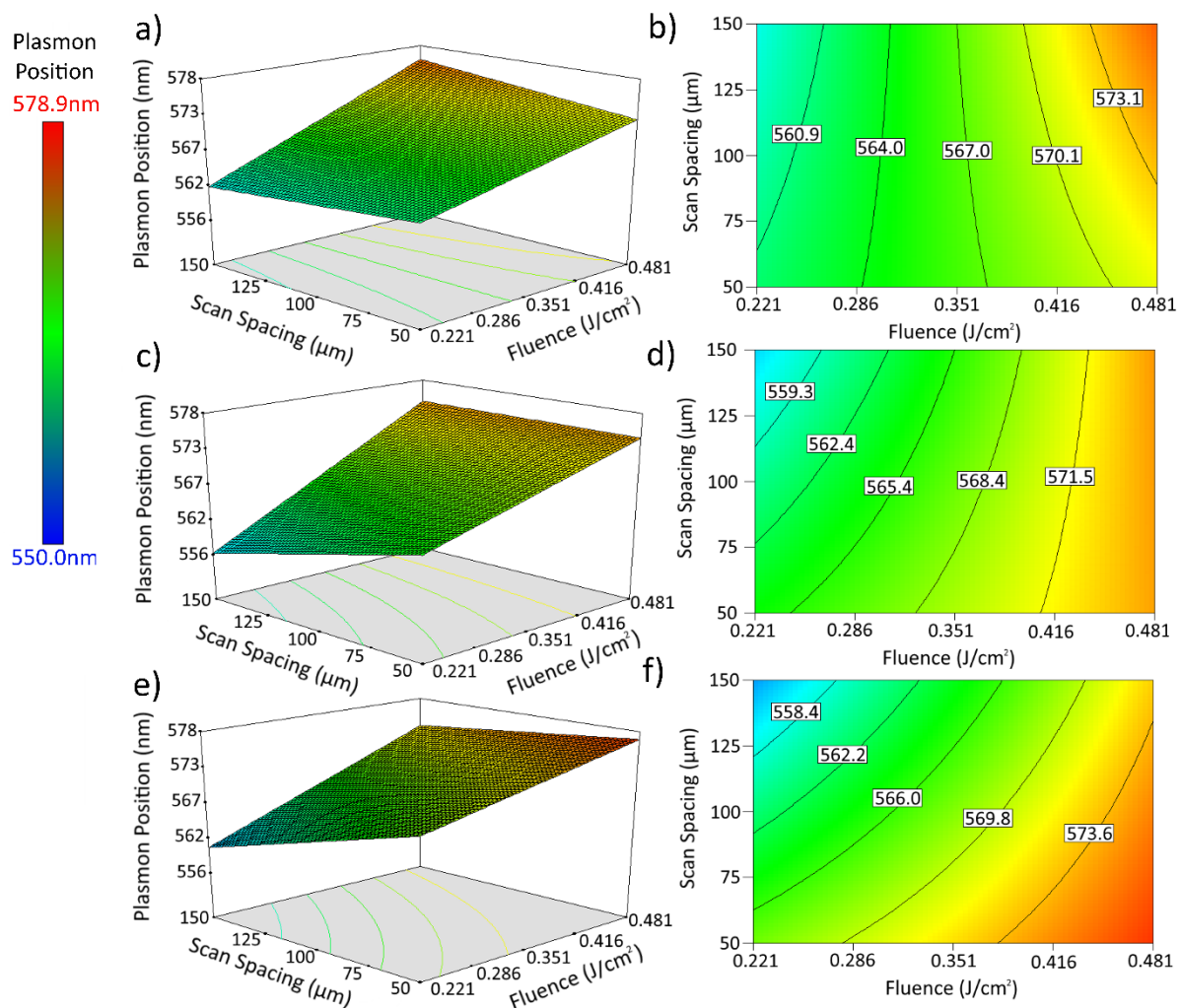### 3.6 Plasmonic Peak Position Model

Similar to the analysis in Section 3.5, a statistically significant model was found describing a relationship between the deposition parameters and the plasmonic peak position ($\lambda_p$) of the resulting film. This model is summarised by the following equation:

$$\lambda_p = 0.91v + 21.1F - 0.06d - 0.008vd + 0.003Fd + 553.05$$

Of the deposition parameters tested, this model denotes the scan speed ($v$), fluence ($F$) and scan spacing ($d$) as the primary determining factors in the observed plasmonic peak position. Based on this equation it is evident that the primary factor influencing the plasmonic peak position is

the fluence imparted during ablation, with higher fluences resulting in films with longer plasmonic wavelengths (Figure 6). In nanostructured materials, longer plasmonic wavelengths are generally known to be a result of larger particle size [34]. As such, this trend suggests that higher fluences may result in either the deposition of larger particles or more melting of the deposited structures, thereby producing larger particles. This observation agrees with the formulae presented in Section 3.5, which also suggest that a higher fluence results in larger particle size. This model also suggests that there are statistically significant scan speed and spacing interactions as well as fluence and scan spacing interactions present in the data, as shown by the vd and Fd components of the equation.



**Fig. 6.** Surface plots and contour plots of the plasmonic peak positions predicted by the derived model at scan speeds of (a,b) 6mm/s, (c,d) 12mm/s and (e,f) 18mm/s.

367    By reviewing the normal plot of residuals and predicted vs actual graphs produced by this
368    model (see Figure 7), it can be seen that the derived equation agrees with the experimental data
369    obtained with no significant outliers in the dataset.
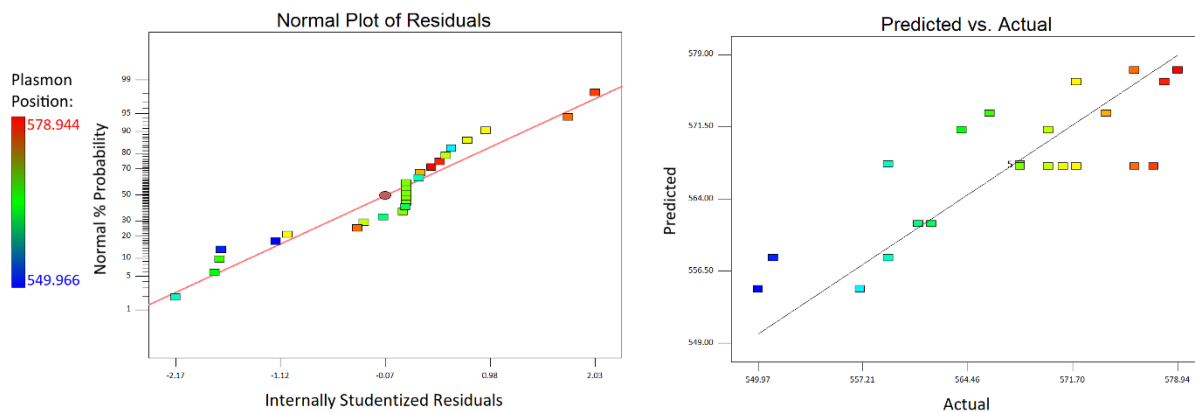


370

371    **Fig. 7.** The normal plot of residuals and predicted vs actual plot for the plasmonic peak position
372    model derived.

373

374    **3.7 Plasmonic Peak Area Model**

375    A statistically significant model was also found describing the area under the plasmonic peak
376    (A) found using integration of each sample in terms of the fluence (F) and scan spacing (d)
377    used during deposition (Figure 8). This relationship can be summarised in the following
378    equation:

379    $A = 44.36F^2 + 0.000081d^2 + 52.34F - 0.070d - 0.12Fd + 15.44$

380    This model proposes that there is a squared relationship between the significant processing
381    parameters and the area under the plasmonic peak. This model also suggests that there are
382    statistically significant interactions between the fluence and scan spacing present, as seen by
383    the presence of the Fd component in the model equation.

20
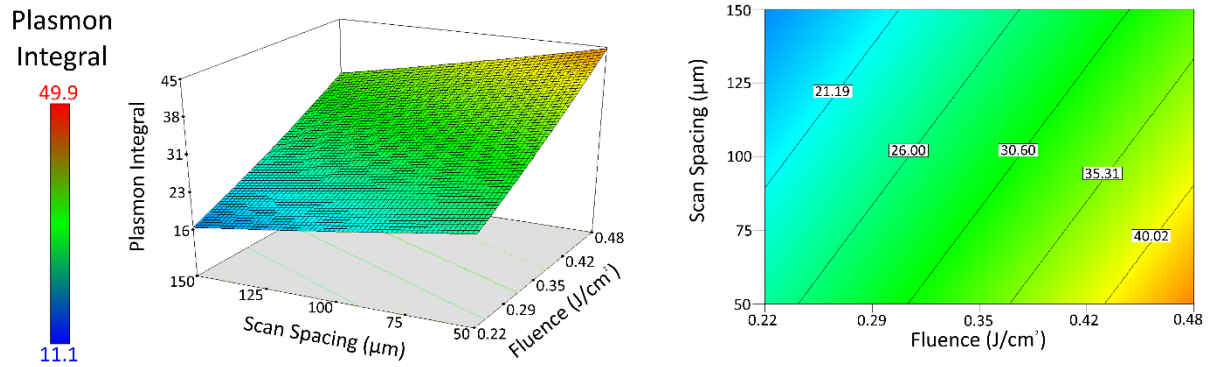
**Fig. 8.** A surface plot and contour plot of the predicted integral (i.e. the predicted area) of the plasmon peaks in terms of the scan spacing and fluence at which samples are produced.

As with the models presented in sections 3.5 and 3.6, a normal plot of residuals and predicted vs actual plot (Figure 9) comparing the data obtained with the predictions of this model were used to evaluate its agreement with observed reality. The normal plot of residuals for this model shows that deviations of observed data from predicted values are mostly normal, with a single apparent outlier (sample number 12) visible in the upper right area of the graph. Similarly, the predicted vs actual graph shows reasonable agreement, with a single apparent outlier on the right-hand side of the graph that is also sample number 12. Sample number 12 was only one of 10 repetitions of the specific set of processing parameters used in its production and the other 9 are in agreement with each other. As such, it seems appropriate to conclude that sample number 12 is simply a statistical outlier in the plasmonic peak integral dataset.
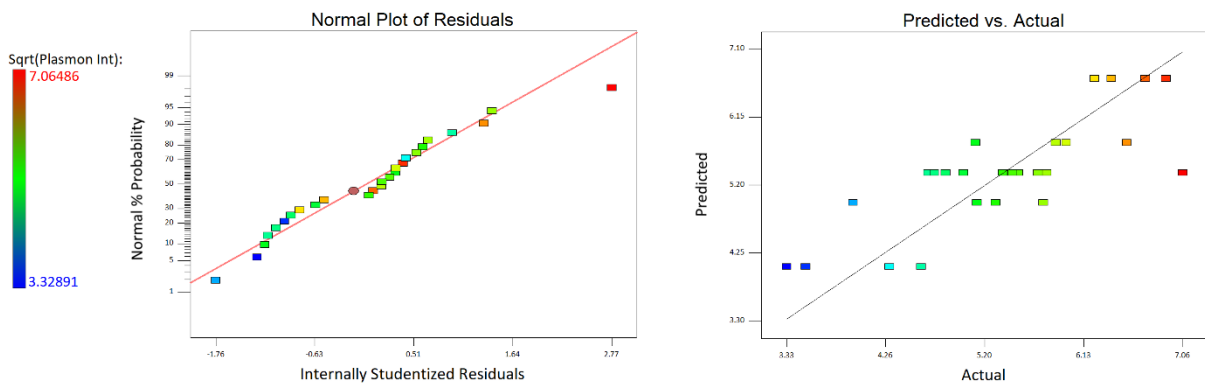


**Fig. 9.** The normal plot of residuals and predicted vs actual plot for the plasmonic peak integral model derived.

## 4. Conclusions

21

402 The use of CAP for rapid, single-step, green deposition of gold nanostructures has been
403 demonstrated. This process results in the deposition of nanostructures with potential
404 applications in sensor development and catalysis due to their high surface area morphology, as
405 observed by SEM. Studies on the resulting surfaces have yielded statistically significant
406 mathematical models describing relationships between the processing parameters and some of
407 the properties of the resulting films.

408 The derived models suggest that the wavelength of the local maximum for the plasmonic peak
409 is primarily determined by the fluence and the scan speed, with a minor role being played by
410 scan-spacing and interactions that are present between the significant parameters. Finally, it
411 was found that the area under this peak is influenced by the fluence and the scan spacing used
412 during sample production with interactions between these parameters also having an influence.

413 SEM imaging of the samples showed a range of structure morphologies and dense packing at
414 all parameters tested. Mathematical models derived suggest that the size and dispersity of the
415 particles deposited (as determined by SEM area measurements and the standard deviation of
416 those measurements) are primarily determined by fluence and interactions between all
417 processing parameters tested. While these models were statistically significant, their
418 significance was not extremely high, suggesting that the parameters tested may not be the
419 primary determiners of particle morphology. It is possible that parameters not investigated
420 (such as ambient temperature and pressure, ambient gas, sample-substrate distance, laser
421 wavelength, pulse repetition frequency and pulse width) may allow for greater control over
422 particle size and film homogeneity than the parameters tested. Future work will likely examine
423 this possibility in more depth. Future process examination via optical emission spectroscopy
424 would also help to confirm or refute a hypothesised link between the mechanisms of CAP and
425 PLD. Optical emission spectroscopy would help to elucidate the specific details of the plume
426 dynamics during CAP which will further facilitate the development and optimisation of this
427 technique.

428

434  **References**

435

436  [1]  Mohammed AM. Fabrication and characterization of gold nano particles for DNA

437       biosensor applications. Chinese Chem Lett 2016;27:801–6.

438       doi:10.1016/j.cclet.2016.01.013.

439  [2]  Peng H, Tang H, Jiang J. Recent progress in gold nanoparticle-based biosensing and

440       cellular imaging. Sci China Chem 2016;59:783–93. doi:10.1007/s11426-016-5570-7.

441  [3]  Zeng S, Yong K-T, Roy I, Dinh X-Q, Yu X, Luan F. A Review on Functionalized

442       Gold Nanoparticles for Biosensing Applications. Plasmonics 2011;6:491–506.

443       doi:10.1007/s11468-011-9228-1.

444  [4]  Anker JN, Hall WP, Lyandres O, Shah NC, Zhao J, Van Duyne RP. Biosensing with

445       plasmonic nanosensors. Nat Mater 2008;7:442–53. doi:10.1038/nmat2162.

446  [5]  Daggumati P, Matharu Z, Seker E. Effect of Nanoporous Gold Thin Film Morphology

447       on Electrochemical DNA Sensing. Anal Chem 2015;87:8149–56.

448       doi:10.1021/acs.analchem.5b00846.

449  [6]  Bouvrée A, D'Orlando A, Makiabadi T, Martin S, Louarn G, Mevellec JY, et al.

450       Nanostructured and nanopatterned gold surfaces: application to the surface-enhanced

451       Raman spectroscopy. Gold Bull 2013;46:283–90. doi:10.1007/s13404-013-0127-4.

452  [7]  Wen Z-Q, Li G, Ren D. Detection of Trace Melamine in Raw Materials Used for

453       Protein Pharmaceutical Manufacturing Using Surface-Enhanced Raman Spectroscopy

454       (SERS) with Gold Nanoparticles. Appl Spectrosc Vol 65, Issue 5, Pp 514-521

455       2011;65:514–21. doi:10.1366/10-06089.

456  [8]  Takale BS, Bao M, Yamamoto Y. Gold nanoparticle (AuNPs) and gold nanopore

457       (AuNPore) catalysts in organic synthesis. Org Biomol Chem 2014;12:2005.

458       doi:10.1039/c3ob42207k.

459  [9]  Gutiérrez L-F, Hamoudi S, Belkacemi K. Synthesis of Gold Catalysts Supported on

460        Mesoporous Silica Materials: Recent Developments. Catalysts 2011;1:97–154.

461        doi:10.3390/catal1010097.

462  [10]  Zhao P, Li N, Astruc D. State of the art in gold nanoparticle synthesis. Coord Chem

463        Rev 2013;257:638–65. doi:10.1016/j.ccr.2012.09.002.

464  [11]  Choy KL. Chemical vapour deposition of coatings. Prog Mater Sci 2003;48:57–170.

465        doi:10.1016/S0079-6425(01)00009-3.

466  [12]  George SM. Atomic Layer Deposition: An Overview. Chem Rev 2010;110:111–31.

467        doi:10.1021/cr900056b.

468  [13]  Emslie DJH, Chadha P, Price JS. Metal ALD and pulsed CVD: Fundamental reactions

469        and links with solution chemistry. Coord Chem Rev 2013;257:3282–96.

470        doi:10.1016/j.ccr.2013.07.010.

471  [14]  Stratakis E, Ranella A, Farsari M, Fotakis C. Laser-based micro/nanoengineering for

472        biological applications. Prog Quantum Electron 2009;33:127–63.

473        doi:10.1016/j.pquantelec.2009.06.001.

474  [15]  Kumar R, Kumar G, Umar A. Pulsed Laser Deposited Nanostructured ZnO Thin

475        Films; A Review. J Nanosci Nanotechnol 2014;14:1911–30.

476        doi:10.1166/jnn.2014.9120.

477  [16]  Piqué A, Kim H, Auyeung RCY, Beniam I, Breckenfeld E. Laser-induced forward

478        transfer (LIFT) of congruent voxels. Appl Surf Sci 2016;374:42–8.

479        doi:10.1016/j.apsusc.2015.09.005.

480  [17]  Dhami G, Tan B, Venketakrishnan K. Laser induced reverse transfer of gold thin film

481        using femtosecond laser. Opt Lasers Eng 2011;49:866–9.

482        doi:10.1016/j.optlaseng.2011.02.019.

483  [18]  Adrian FJ, Bohandy J, Kim BF, Jette AN, Thompson P. A study of the mechanism of

484        metal deposition by the laser-induced forward transfer process. J Vac Sci Technol B

485        1987;5:1490–4. doi:10.1116/1.583661.

486  [19]  Henley SJ, Carey JD, Silva SRP. Pulsed-laser-induced nanoscale island formation in

487        thin metal-on-oxide films. Phys Rev B - Condens Matter Mater Phys 2005;72:1–10.

488     doi:10.1103/PhysRevB.72.195408.

489     [20]    Trice J, Thomas D, Favazza C, Sureshkumar R, Kalyanaraman R. Pulsed-laser-
490             induced dewetting in nanoscopic metal films: Theory and experiments. Phys Rev B -
491             Condens Matter Mater Phys 2007;75:1–15. doi:10.1103/PhysRevB.75.235439.

492     [21]    Ruffino F, Pugliara A, Carria E, Romano L, Bongiorno C, Spinella C, et al. Novel
493             approach to the fabrication of Au/silica coreshell nanostructures based on nanosecond
494             laser irradiation of thin Au films on Si. Nanotechnology 2012;23. doi:10.1088/0957-
495             4484/23/4/045601.

496     [22]    Lu L-X, Wang Y-M, Srinivasan BM, Asbahi M, Yang JKW, Zhang Y-W.
497             Nanostructure Formation by controlled dewetting on patterned substrates: A combined
498             theoretical, modeling and experimental study. Sci Rep 2016;6:32398.
499             doi:10.1038/srep32398.

500     [23]    Pandey P, Kunwar S, Sui M, Bastola S, Lee J. Role of annealing temperature, time,
501             and composition on the fabrication of AUxPd1-xnanostructures on c-plane sapphire by
502             the solid-state dewetting of bimetallic thin films. IEEE Trans Nanotechnol
503             2018;17:325–31. doi:10.1109/TNANO.2018.2801943.

504     [24]    McCann R, Hughes C, Bagga K, Stalcup A, Vázquez M, Brabazon D. Pulsed laser
505             deposition of plasmonic nanostructured gold on flexible transparent polymers at
506             atmospheric pressure. J Phys D Appl Phys 2017;50:245303.

507     [25]    Kwok H., Kim H., Kim D., Shen W., Sun X., Xiao R. Correlation between plasma
508             dynamics and thin film properties in pulsed laser deposition. Appl Surf Sci 1997;109–
509             110:595–600. doi:10.1016/S0169-4332(96)00640-X.

510     [26]    Donnelly T, Lunney JG. Confined laser ablation for single-shot nanoparticle
511             deposition of silver. Appl Surf Sci 2013;282:133–7. doi:10.1016/j.apsusc.2013.05.083.

512     [27]    Nikov RG, Dikovska AO, Nedyalkov NN, Avdeev G V., Atanasov PA. Au
513             nanostructure fabrication by pulsed laser deposition in open air: Influence of the
514             deposition geometry. Beilstein J Nanotechnol 2017;8:2438–45.
515             doi:10.3762/bjnano.8.242.

516     [28]    Rajendiran S, Rossall AK, Gibson A, Wagenaars E. Modelling of laser ablation and

517        reactive oxygen plasmas for pulsed laser deposition of zinc oxide. Surf Coatings
518        Technol 2014;260:417–23. doi:10.1016/j.surfcoat.2014.06.062.

519   [29]   Jimenez A, Lepage D, Beauvais J, Dubowski JJ. Study of surface morphology and
520        refractive index of dielectric and metallic films used for the fabrication of
521        monolithically integrated surface plasmon resonance biosensing devices.
522        Microelectron Eng 2012;93:91–4. doi:10.1016/j.mee.2011.10.016.

523   [30]   Sharma R, Ragavan K V, Thakur MS, Raghavarao KSMS. Recent advances in
524        nanoparticle based aptasensors for food contaminants. Biosens Bioelectron
525        2015;74:612–27. doi:10.1016/j.bios.2015.07.017.

526   [31]   Schindelin J, Arganda-Carreras I, Frise E, Kaynig V, Longair M, Pietzsch T, et al. Fiji:
527        an open-source platform for biological-image analysis. Nat Methods 2012;9:676–82.
528        doi:10.1038/nmeth.2019.

529   [32]   Yamaguchi M, Araga S, Mita M, Yamasaki K, Maekawa K. On-Demand Infrared
530        Laser Sintering of Gold Nanoparticle Paste for Electrical Contacts. IEEE Trans
531        Components, Packag Manuf Technol 2015;5:1160–8.
532        doi:10.1109/TCPMT.2015.2450312.

533   [33]   Ansari SA, Husain Q. Potential applications of enzymes immobilized on/in nano
534        materials: A review. Biotechnol Adv 2012;30:512–23.
535        doi:10.1016/j.biotechadv.2011.09.005.

536   [34]   Huang X, El-Sayed MA. Gold nanoparticles: Optical properties and implementations
537        in cancer diagnosis and photothermal therapy. J Adv Res 2010;1:13–28.
538        doi:10.1016/j.jare.2010.02.002.

539   [35]   Maye MM, Han L, Kariuki NN, Ly NK, Chan W Ben, Luo J, et al. Gold and alloy
540        nanoparticles in solution and thin film assembly: Spectrophotometric determination of
541        molar absorptivity. Anal Chim Acta 2003;496:17–27. doi:10.1016/S0003-
542        2670(03)00986-3.

543   [36]   McCann R, Bagga K, Groarke R, Stalcup A, Vázquez M, Brabazon D. Microchannel
544        fabrication on cyclic olefin polymer substrates via 1064nm Nd:YAG laser ablation.
545        Appl Surf Sci 2016;387:603–8. doi:10.1016/j.apsusc.2016.06.059.

546    [37]   O'Neil CE, Taylor S, Ratnayake K, Pullagurla S, Singh V, Soper SA. Characterization
547          of activated cyclic olefin copolymer: effects of ethylene/norbornene content on the
548          physiochemical properties. Analyst 2016;141:6521–32. doi:10.1039/C6AN01448H.

549    [38]   Stathaki T. Image Fusion: Algorithms and Applications. 1st ed. Elsevier; 2008.

550    [39]   Gonzalez RC, Woods RE. Digital Image Processing. 3rd ed. Pearson; 2007.

551    [40]   Voigtman E. Comparison of Signal-to-Noise Ratios. Anal Chem 1997;69:226–34.
552          doi:10.1021/ac960675d.

553    [41]   Patty A, Peijiang Z. Advances in Materials Sciences, Energy Technology and
554          Environmental Engineering : Proceedings of the International Conference on Materials
555          Science, Energy Technology and Environmental Engineering, MSETEE 2016, Zhuhai,
556          China, May 28-29, 2016. CRC Press; 2016.

557